NASA/TM—2016-218878

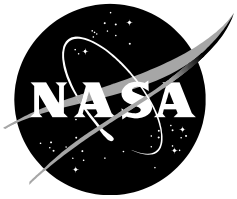

The Transition From Thick to Thin Plate Wake Physics: Whither Vortex Shedding?

Man Mohan Rai
Ames Research Center
Moffett Field, CA-94035

March 2016

NASA STI Program ... in Profile

Since its founding, NASA has been dedicated to the advancement of aeronautics and space science. The NASA scientific and technical information (STI) program plays a key part in helping NASA maintain this important role.

The NASA STI program operates under the auspices of the Agency Chief Information Officer. It collects, organizes, provides for archiving, and disseminates NASA's STI. The NASA STI program provides access to the NTRS Registered and its public interface, the NASA Technical Reports Server, thus providing one of the largest collections of aeronautical and space science STI in the world. Results are published in both non-NASA channels and by NASA in the NASA STI Report Series, which includes the following report types:

- TECHNICAL PUBLICATION. Reports of completed research or a major significant phase of research that present the results of NASA Programs and include extensive data or theoretical analysis. Includes compilations of significant scientific and technical data and information deemed to be of continuing reference value. NASA counterpart of peer-reviewed formal professional papers but has less stringent limitations on manuscript length and extent of graphic presentations.

- TECHNICAL MEMORANDUM. Scientific and technical findings that are preliminary or of specialized interest, e.g., quick release reports, working papers, and bibliographies that contain minimal annotation. Does not contain extensive analysis.

- CONTRACTOR REPORT. Scientific and technical findings by NASA-sponsored contractors and grantees.

- CONFERENCE PUBLICATION. Collected papers from scientific and technical conferences, symposia, seminars, or other meetings sponsored or co-sponsored by NASA.

- SPECIAL PUBLICATION. Scientific, technical, or historical information from NASA programs, projects, and missions, often concerned with subjects having substantial public interest.

- TECHNICAL TRANSLATION. English-language translations of foreign scientific and technical material pertinent to NASA's mission.

Specialized services also include organizing and publishing research results, distributing specialized research announcements and feeds, providing information desk and personal search support, and enabling data exchange services.

For more information about the NASA STI program, see the following:

- Access the NASA STI program home page at http://www.sti.nasa.gov

- E-mail your question to help@sti.nasa.gov

- Phone the NASA STI Information Desk at 757-864-9658

- Write to:
  NASA STI Information Desk
  Mail Stop 148
  NASA Langley Research Center
  Hampton, VA 23681-2199

NASA/TM-2016-218878

The Transition From Thick to Thin Plate Wake Physics: Whither Vortex Shedding?

Man Mohan Rai
Ames Research Center
Moffett Field, California

National Aeronautics and
Space Administration

Ames Research Center
Moffett Field, California 94035-1000

March 2016

THE TRANSITION FROM THICK TO THIN PLATE WAKE PHYSICS: WHITHER VORTEX SHEDDING?

Man Mohan Rai[1]
NASA Ames Research Center, Moffett Field, CA-94035

ABSTRACT

The near and very near wake of a flat plate with a circular trailing edge is investigated with data from direct numerical simulations. Computations were performed for six different combinations of the Reynolds numbers based on plate thickness (D) and boundary layer momentum thickness upstream of the trailing edge (θ). Unlike the case of the cylinder, these Reynolds numbers are independent parameters for the flat plate. The separating boundary layers are turbulent in all the cases investigated. One objective of the study is to understand the changes in the wake vortex shedding process as the plate thickness is reduced (increasing θ/D). The value of D varies by a factor of 16 and that of θ by approximately 5 in the computations. Vortex shedding is vigorous in the low θ/D cases with a substantial decrease in shedding intensity in the large θ/D cases. Other shedding characteristics are also significantly altered with increasing θ/D. A visualization of the shedding process in the different cases is provided and discussed. The basic shedding mechanism is explored in depth. The effect of changing θ/D on the time-averaged, near-wake velocity statistics is also discussed. A functional relationship between the shedding frequency and the Reynolds numbers mentioned above is obtained.

INTRODUCTION

Cylinder wakes with large-scale shed vortices have been investigated extensively over several decades. Numerous reviews exist in the literature. The process of shedding has been probed via instantaneous limiting streamlines, critical points and corresponding flow patterns by Perry, Chong & Lim (1982) for the cylinder and by Perry & Steiner (1987) for a flat plate (held normal to the flow direction and at an angle). Shedding has also been investigated from the perspective of stability analysis; this however is not the approach pursued in the present investigation. The Reynolds number of interest in the case of the cylinder is based on the diameter D, Re_D. The changes in flow features that are observed, as this one parameter is increased/decreased, are myriad and continue to be the subject of experimental, computational and theoretical research.

The objective of the present investigation is to better understand the shedding process in the wake of a flat plate with a circular trailing edge and turbulent separating boundary layers; in particular changes in shedding and related wake characteristics as the plate becomes very thin in relation to the boundary layer thickness. Unlike the case of the cylinder, the Reynolds number based on momentum thickness of the boundary layer just upstream of the trailing (Re_{θ}) and the Reynolds number defined using the thickness of the flat plate or the diameter of its trailing edge (Re_D), are independent parameters. The data used in the present investigation are obtained from direct numerical simulations (DNSs) of flat plate flow for six different combinations of these two Reynolds numbers. The turbulent boundary layers and the wake are all computed via DNS. The separating boundary layers are statistically identical. Therefore the wake is symmetric in the mean. Here we continue the analysis of the near wake of the flat plate initiated in Rai (2013, 2014 & 2015).

---

[1] Senior Scientist for Computational Sciences, Exploration Technology Directorate.

The wake of the thin plate with turbulent boundary layers and a sharp trailing edge has been discussed in numerous articles, one of the earliest being that of Chevray & Kovasznay (1969). The ratio of the boundary layer momentum thickness to the trailing edge thickness of the plate (θ/D) is 23.2 in their study. The boundary layers merge to form the wake and shedding is absent. In contrast, the thick plates with a circular trailing edge (small θ/D cases), investigated by the present author (Rai, 2013, 2014 & 2015), exhibit vigorous vortex shedding. In the present investigation we seek to understand the transition in shedding characteristics from the vigorously shedding small θ/D cases to the weakly shedding large θ/D cases. Changes in, for example, the coherence of the shed vortices (in the spanwise direction), centerline velocity spectra, time-averaged velocity statistics, the basic shedding mechanism and shedding frequency are all topics of interest and are discussed in this article. Some of the reasons underlying the substantial changes in the observed flow features as θ/D is increased, are also provided. A functional relationship between shedding frequency and Re_{θ} and Re_D, obtained using the DNS data, is proposed for the range of Reynolds numbers considered.

Cylinder Vortex Shedding

Prior to embarking on the very complex shedding process that occurs in the case of flat plates with turbulent separating boundary layers, it seems appropriate to examine vortex shedding in the case of cylinders at low Reynolds numbers. Accordingly, a computation of cylinder flow at Re_D = 195 was performed on the grid utilized in Rai (2010a) for the Case Re_D = 3900. The computational method used is the same as in Rai (2010a). The results presented below were obtained after the initial transients had subsided and a time-periodic flow was established.

As mentioned earlier, Perry, Chong & Lim (1982) provide an analysis of the vortex shedding process for the flow past a cylinder. The authors use limiting streamlines to obtain the flow pattern at eight different phases of the shedding process (Fig. 2 in their article). The various patterns encountered, and the presence of critical points and “alleyways” for fluid transport are discussed. However, while their findings provide some of our earliest and important insights into the shedding process, a discussion of the events that lead to the formation of a shed vortex is not provided. In the present study we ask the following questions: What are the events that result in the initial circulating flow and associated center? What role does the velocity field induced by the previously shed vortex (or two) play in the shedding of the subsequent vortex? Does the shear-layer play a role as well? Does the associated minimum in pressure appear at the same time as the circulating flow or later? The answers are provided below.

In the following figures we focus on three different phases, ϕ_A (prior to appearance of circulating flow), ϕ_B (soon after the appearance of circulating flow), and ϕ_C (soon after the appearance of the associated pressure minimum), $\phi_A < \phi_B < \phi_C$. Figure 1a shows instantaneous velocity vectors, and pressure contours showing the pressure minimum associated with the relatively well-formed upper vortex (clockwise rotation) at the phase ϕ_A. The flow in the region below the centerline is largely downward with the area near the base showing flow towards the base that then curves sharply and subsequently points downstream. Figure 1b is an enlarged view of the region within the rectangle in Fig. 1a; it confirms the observation that circulating flow is not observed at this phase. The downward flow very near the base is a remnant of the flow induced by the previous *positive shed vortex*. Further away from the base the downward flow is induced by the upper negative vortex and also the previously shed positive vortex.

Figures 2a and 2b are the counterparts of Figs 1a and 1b, but at the phase ϕ_B. Here we see the first signs of circulating flow within the rectangle in Fig. 2a. This circulatory flow is clearly visible in Fig. 2b. The question that arises then is, what causes the flow to circulate and exhibit a center? Close to the base we continue to observe downward flow caused by the previous positive shed vortex. Comparing the pressure contours in Figs. 1a & 2a, it is clear that the upper negative vortex has moved to the right and downward with increasing phase. The downward movement of this vortex causes it to have a greater influence on the flow below the centerline. Its movement to the right causes the flow near the base and below the centerline to turn upward and to the left. The flow in the lower shear layer, and even further

below, continues to point in the positive x direction. We now have all the constituents for circulatory flow: downward flow very near the base, reverse flow below the centerline and forward flow in the shear layer. The upward motion caused by the upper vortex (left of its center) causes the shear layer flow also to turn slightly upward. The end result is circulating flow very near the base and a saddle point to its right. Thus, the flow induced by the two previous shed vortices (negative/positive) together with the forward flow in the shear layer, are directly responsible for the initiation of circulating flow. A contour plot of instantaneous pressure with a large number of contours did not show any evidence, or tendency toward, a minimum in pressure at the phase ϕ_B.

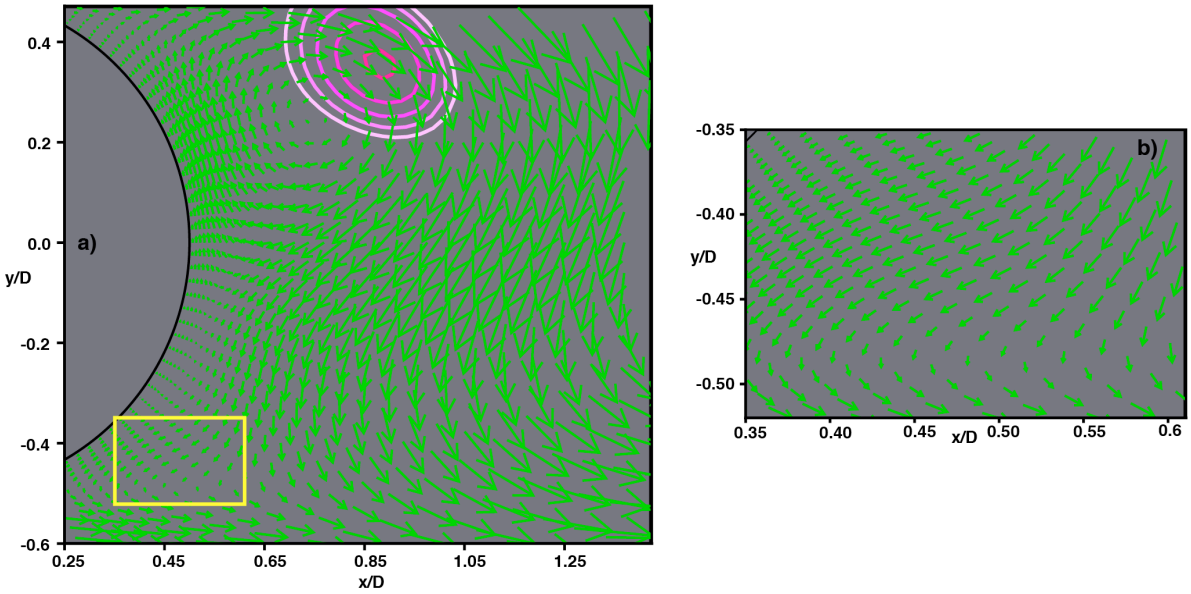

Figure 1. Velocity vectors and pressure contours at $\phi = \phi_A$.

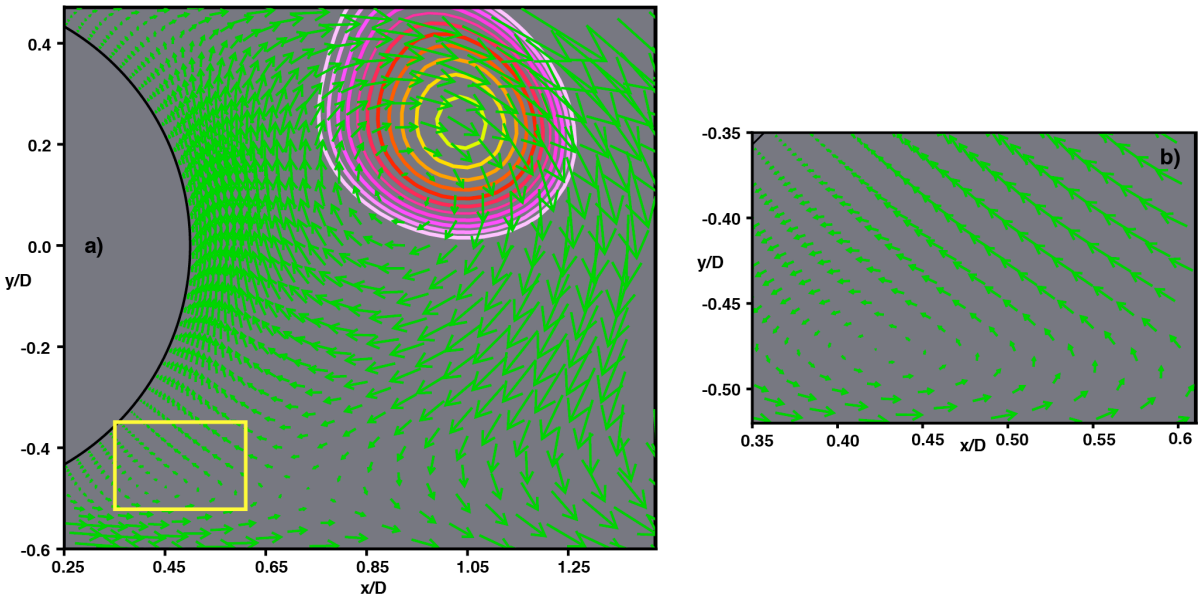

Figure 2. Velocity vectors and pressure contours at $\phi = \phi_B$.

Figures 3a and 3b are also counterparts of Figs. 1a and 1b, but at the phase ϕ_C. The circulatory flow is evident. However, instantaneous pressure contours at this phase show a minimum (marked with an x in Fig. 3a and with both an x and pressure contours in Fig. 3b). The center of rotation and the pressure minimum are at slightly different locations. Subtracting the velocity at the pressure minimum from the velocity field and redrawing the velocity vectors (being in a frame of reference moving with the velocity of the pressure minimum) moves the center to the pressure minimum but little else. At later phases the center and pressure minimum move to the right, the shear-layer shows a distinct roll-up and the new vortex strengthens. With this basic understanding of the vortex formation process in a relatively simple case, it remains to be seen if the flat plate with turbulent separating boundary layers also exhibits similar shedding characteristics and if these characteristics persist as θ/D is increased.

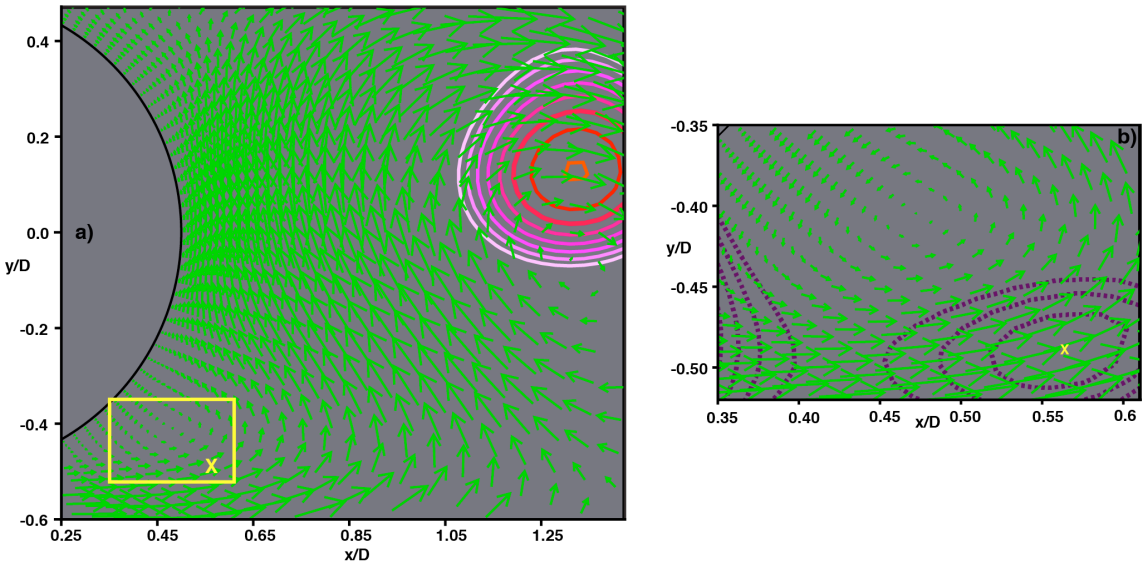

Figure 3. Velocity vectors and pressure contours at $\phi = \phi_C$.

PLATE COMPUTATIONAL GRID, FLOW/GEOMETRY PARAMETERS AND NUMERICAL METHOD

The computational region for the flat plate DNSs is divided into two zones to facilitate grid generation and provide adequate grid resolution for the wake. Figure 4 shows the plate cross-section and the two zones that comprise the computational region. The three-dimensional zones and grids are obtained by uniformly spacing copies of these two-dimensional zones in the spanwise direction (z). The plate zone is bounded by four boundaries: the plate surface (excluding the trailing edge), an external boundary and, two zonal boundaries (top and bottom) that interface with the wake zone. The plate zone captures the inviscid flow-field upstream of the trailing edge and the plate boundary layers. The leading edge of the plate is an ellipse. The wake zone is constructed to provide adequate grid resolution for the detached shear layers, the recirculation region and the wake. The boundaries of this zone include the circular trailing edge, the upper and lower boundaries and the exit boundary. Both the upper and lower boundaries consist of a zonal boundary segment that interfaces with the plate zone and a second segment that serves as an external boundary. Direct numerical simulations for six different combinations of Re_L (Reynolds number based on plate length L) and Re_D were performed to obtain the data used in this study (Cases A - F). Of these, only Cases E & F were computed as a part of the current effort.

The placement of the various boundaries in relation to the plate surface in Cases A - D is provided in Rai (2013, 2014 & 2015). The vertical extent of the wake zone near the trailing edge, where its upper/lower boundaries are horizontal is large enough to completely contain the wake in all cases (Fig. 4 in Rai 2013 clearly shows the adequacy of this dimension in Case A). The spanwise extent of the region

in Cases A - D is 4.0D. Values of Re_L and Re_D for Cases A – D were chosen to be the vertices of a rectangle in Re_L - Re_D space in the order ACBDA (counter-clockwise direction, Case A corresponds to the upper right-hand corner). *Cases A - D of the present study are labeled as A - D in Rai (2015) as well.*

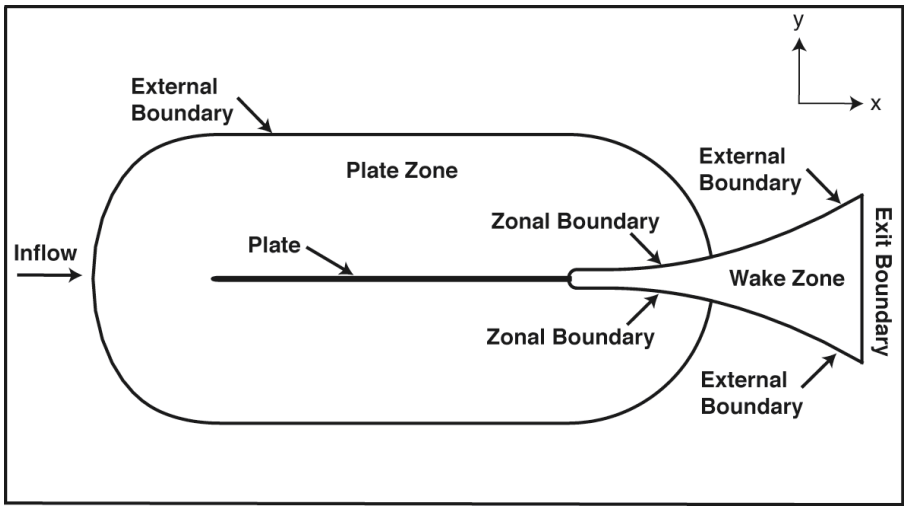

Figure 4. Midspan plate section and multiple zone discretization of the computational region (Rai 2013).

Figure 5a shows representative grids in the vicinity of the trailing edge in both zones. These grids were generated with an algebraic grid generator. Both the grids have the same spacing in the wall normal direction at the plate surface.

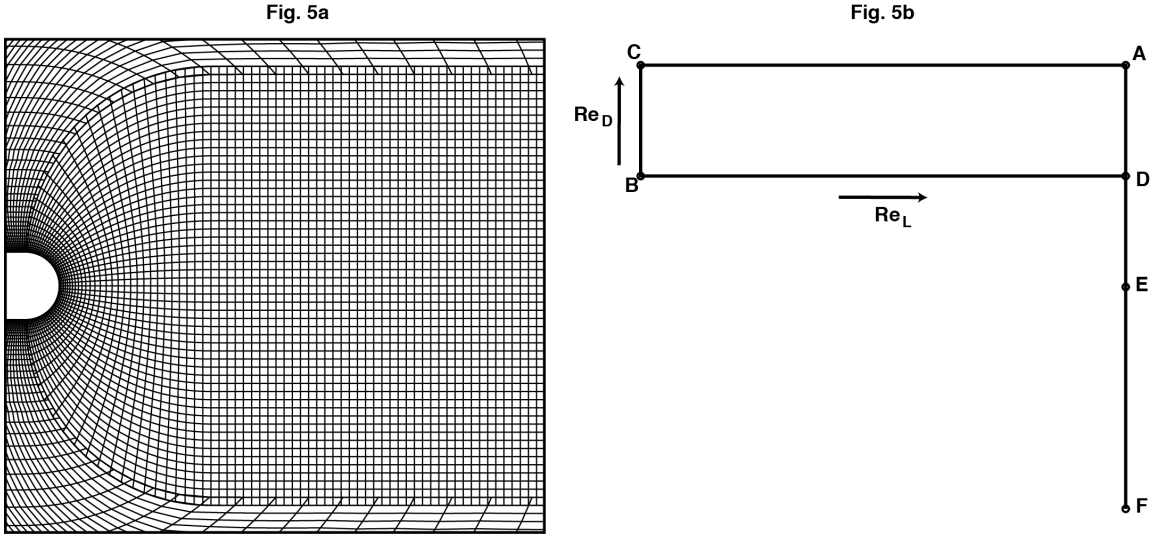

Figure 5. a) Representative grids in the plate and wake zones in the trailing edge region (Rai 2013) and b) Cases A – F in Re_L - Re_D space (not drawn to scale).

The grid in the wake zone transitions from curvilinear near the trailing edge to rectangular downstream. In Cases A, C & D, downstream of x/D ≈ 13.5, the wake grid coarsens gradually in the x direction. In Case B grid coarsening begins at x/D = 8.5. In addition to reducing the computational costs, this coarsening dissipates the wake to a degree that inviscid exit boundary conditions can be employed at the exit boundary of the wake zone. The wake grid for Case A was constructed with 741 grid points in the

streamwise direction, 411 in the cross-stream direction and 256 in the spanwise direction (about 78 x 10^6 grid points). The resolution achieved along the centerline in the three spatial directions at x/D = 10.0 is approximately Dx/h = 3.7, Dy/h = 2.2 and Dz/h = 2.1 where h is the computed Kolmogorov length scale at the same location. The grid resolution in the plate grid in the x, y and z directions for this case is about 17.8, 0.84 and 6.6 wall units respectively, based on the wall shear velocity near the end of the plate. The resolution achieved in all six cases reported here is similar.

The primary goal in the current investigation is to study the effect of increasing θ/D on the vortex shedding process. Accordingly, the thickness of the plate in Cases E and F was reduced by factors of 2 & 8, respectively, from that used in Case D. The length of the plate in Cases E & F was the same as in Cases A & D. Figure 5b is a schematic of the six cases in Re_L - Re_D space (not drawn to scale). In Cases E and F the *physical dimension* of the computational region in the z direction (Δz) was kept the same as in Case D to ensure that the computed statistics on the plate were not affected by the imposition of periodicity in the z direction. However, the thickness of the plate was reduced as mentioned earlier. This resulted in the z dimension of the computational region being 8.0D and 32.0D in Cases E & F, respectively. The grid resolution in the z direction, however, is the same as in Case D. For the same reason (an accurate simulation/representation of the boundary layer), the vertical extent (physical) of the wake region (in the region where the upper and lower boundaries are horizontal) was also maintained at approximately the same value as in Case D; the grid resolution is approximately the same. The same reasoning was also used in the placement of the external boundary of the plate zone and the exit boundary of the wake zone in Cases E & F (in terms of the plate thickness they were placed approximately 2 and 8 times further away compared to Case D). The grid spacing in the wall-normal direction in Cases E & F is half that used in Cases A – D to better resolve the smaller trailing edges. Values of Re_L & Re_D for all the cases are provided in Table 1.

	Plate length	Re_L & Re_D
Case A	125.50D	1,255,000 & 10,000
Case B	60.50D	302,500 & 5000
Case C	30.25D	302,500 & 10,000
Case D	251.00D	1,255,000 & 5000
Case E	502.00D	1,255,000 & 2500
Case F	2008.00D	1,255,000 & 625

Table 1. Plate length, Re_L and Re_D for Cases A - F.

The high-order accurate upwind-biased method developed in Rai (2008, 2010b) is used here to compute the flow over the plate as well as that in the wake. The inviscid terms are computed using sixth- and seventh-order upwind-biased finite differences, both with seventh-order dissipation terms. The viscous terms are computed with fourth-order central differences. The method is iterative-implicit in nature, multiple iterations are employed at each time-step to solve the nonlinear finite-difference equations arising from a fully implicit formulation; the method is second-order accurate in time. As discussed above the computational region is discretized using the plate grid and the wake grid. The boundaries that contain these grids can be broadly classified as natural and zonal boundaries. The natural boundaries include the external boundary of the plate grid, the surface of the plate, the exit boundary of the wake grid, the segments of the upper and lower boundaries of the wake grid labeled as "external boundary" in Fig. 4, and, the boundaries in the *z* direction. The upstream segment of the upper boundary between the plate and wake grids is an example of the zonal boundaries used in the computation. Periodic boundary conditions are imposed on the boundaries in the *z* direction (homogeneity in *z*). No-slip/adiabatic wall conditions are used on the plate surface. Wall blowing/suction is implemented on a short segment on both the upper and lower surfaces of the plate to induce transition to turbulence. The boundary layer is turbulent upstream of the trailing edge. The upper and lower transitional/turbulent boundary layers and the wake are all computed via DNS. The natural and zonal boundary conditions used here are discussed in Rai (2010b).

RESULTS

The data provided in the following figures were obtained during the data-sampling period (after the initial transients were eliminated). The time-step n = 0 corresponds to the time at which sampling was initiated. In the following contour plots the colors blue/green represent negative values (deep blue representing the lowest value) of the term/quantity being discussed. Orange, red and magenta represent positive values (magenta bordering on white representing the highest value). Shades of yellow represent values close to zero. The approach taken here is to use the test case (A, B, C, D, E or F) that highlights the attribute that is being discussed, followed as necessary by appropriate remarks regarding the same attribute as it appears in the remaining cases. Velocity statistics etc. were obtained over 160 shedding periods for Cases A & C, 200 shedding periods for Cases B & D, 180 for Case E and 430 for Case F. The time-step used in cases A - D is approximately $U\Delta\tau/D = 0.0033$; this corresponds to about 1750 time steps per shedding period in Case A. The time step used in cases E and F is half as much (the grid spacing at the wall in the wall-normal direction for these two cases is half that used in Cases A – D).

Flow Visualization for Cases A, D & E

We begin the investigation of shed vortex structure, and the manner in which it changes with increasing (θ/D), in Cases A, D & E with a top view of surfaces of constant pressure (Fig. 6). Figure 6a shows an instantaneous constant pressure surface for Case A. The shed vortices are clearly observed as nearly cylindrical regions of low pressure. They show little distortion in the z direction.

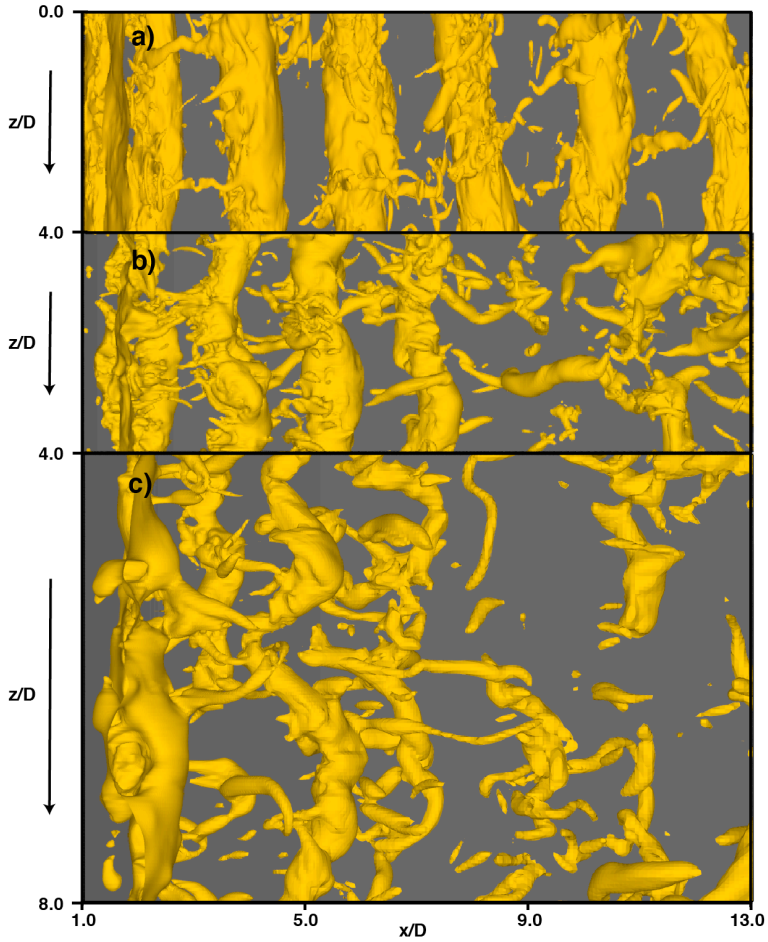

Figure 6. Instantaneous surfaces of constant pressure (top-view), a) Case A (n = 70000), b) Case D (n = 180,000), c) Case E (n = 192,000).

The rib vortices in the braid regions connecting consecutive shed vortices of opposite sign are also evident as narrow tubes; some of them are highly distorted. Shed vortices that are ruptured or that show large distortions are rare in Case A (one ruptured vortex was identified and reported in Rai (2013) for Case A). Figure 8b shows an instantaneous constant pressure surface for Case D. The larger spanwise distortions near the base region (in comparison to Case A) and what appears to be the beginning of vortex breakdown further downstream is evident (less structured shedding as θ/D increases by about a factor of 2). Because it is tempting to consider this loss in coherency as solely due to vortex breakdown processes, we hasten to add that the complexity in vortex structure is sometimes evident at shed vortex inception very near the trailing edge. This is an indication that, at times, the formation process itself varies considerably from the norm. The underlying reasons will become evident in the figures that follow.

Case E (Fig. 6c, which involves a further increase of θ/D) yields significant vortex distortion in the entire near-wake region. Obtaining phase-averaged statistics in this case is difficult because of this distortion and reasons relating to cross-sectional structure of the shed vortices. It is clear from Figs. 6a – 6c that increasing θ/D beyond a certain level results in the loss of coherence of shed vortices. We note here that the spanwise dimension in Case E is 8.0D whereas in Case D it is 4.0D although the actual physical extent is the same in these two cases.

The loss in coherence of the shed vortices with increasing θ/D has an effect on the induced cross-stream velocity (v) at the wake center-plane (y/D = 0.0). Figures 7a and 7b show contours of instantaneous v for Cases A and D respectively, at the same time instants as in Figs. 6a and 6b. Figure 7a shows bands of positive and negative v, caused by the passage of successive shed vortices, that are nearly vertical but with considerable small-scale structure. In Fig. 7b the band structure begins to show waviness in the z direction and incursions of positive regions into negative bands and vice versa past the location x/D $\approx$ 7 (Case D).

To better understand the loss in coherence with increasing θ/D, we resort to side views of spanwise vorticity for the two extreme cases discussed thus far, Cases A and E. Figure 8a shows contours of instantaneous spanwise vorticity for Case A. As mentioned in Rai (2014), the shed vortex at inception (in this instance the lower one) is not a single cylindrical vortex as in low Reynolds number cylinder flows. Instead, it is an amalgam of several smaller vortices of both signs. Vortices of the same sign as the vorticity in the shear layer that is rolling up are dominant. In addition segments of the shear layer and shear-layer vortices are incorporated in the newly forming vortex. Figure 8b shows instantaneous spanwise vorticity contours for Case E. The differences between Figs. 8a and 8b are striking. Firstly, we observe that relative to the thickness of the plate, the thickness of the detached shear layers in Case E is considerably larger than in Case A. As mentioned in Rai (2014 & 2015) the region where the contours are clustered does not include the log-layer. The log-layer eddies convect past the trailing edge and may then be assimilated by the shed vortices (for sufficiently small values of θ/D). Secondly, much of the small-scale activity seen in Fig. 8a is absent in Fig. 8b.

The third and perhaps the most important difference is that the two detached shear layers (DSLs) in Fig. 8b are separated by a physical distance that is approximately one quarter of that in Fig. 8a (the trailing edge diameter in Case E is 0.25 times that in Case A). The smaller separation results in a stronger interaction between the DSLs in Case E. In addition, at times there is less room for a more conventional, approximately circular, roll-up of the DSLs as in Case A. Instead, a folding of the DSL into two distinct layers occurs as in Fig. 8b. As a result of the strong interaction, the shed vortex is initially stretched out in the x direction and sometimes breaks up into multiple shed vortices that occasionally reconstitute into a single larger shed vortex. The end result is the lack of coherence seen in Fig. 6c.

Figures 9a and 9b show contours of instantaneous spanwise vorticity at a given instant but at z/D = 0.0 and at z/D = 4.0 (midspan) for Case E. The primary positive vortex occurs at approximately x/D = 2.0 in Fig. 9a but at x/D = 2.7 in Figure 9b (see arrows). At x/D = 2.7 in Fig. 9a we only have a relatively

undisturbed shear layer. Figures 9a and 9b once again show the lack of coherence in the z direction and also that, occasionally the shed vortices, even in Case E, are approximately circular.

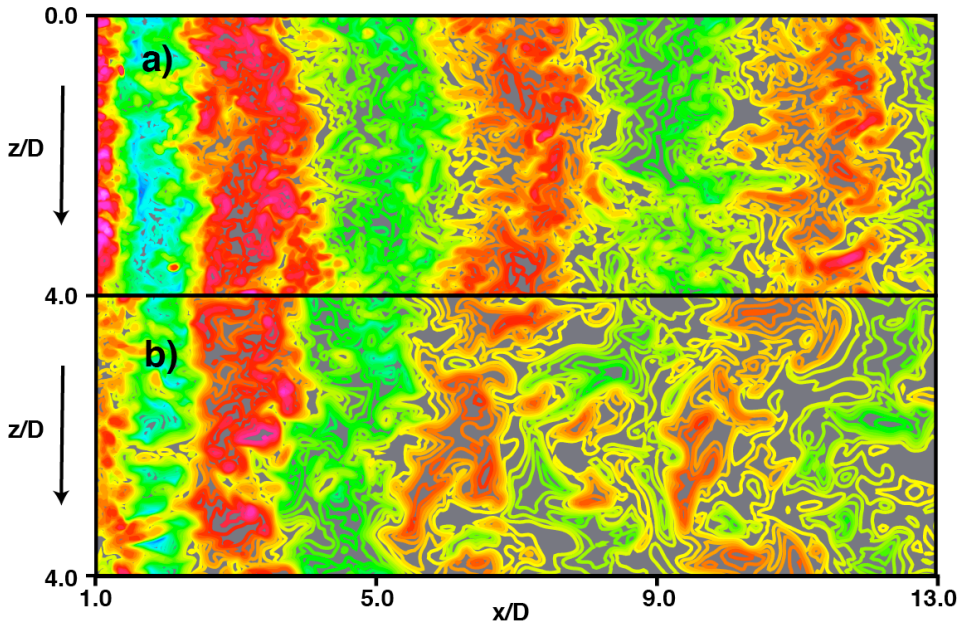

Figures 7. Instantaneous contours of cross-stream velocity in the wake center-plane, a) Case A (n = 70000), b) Case D (n = 180,000).

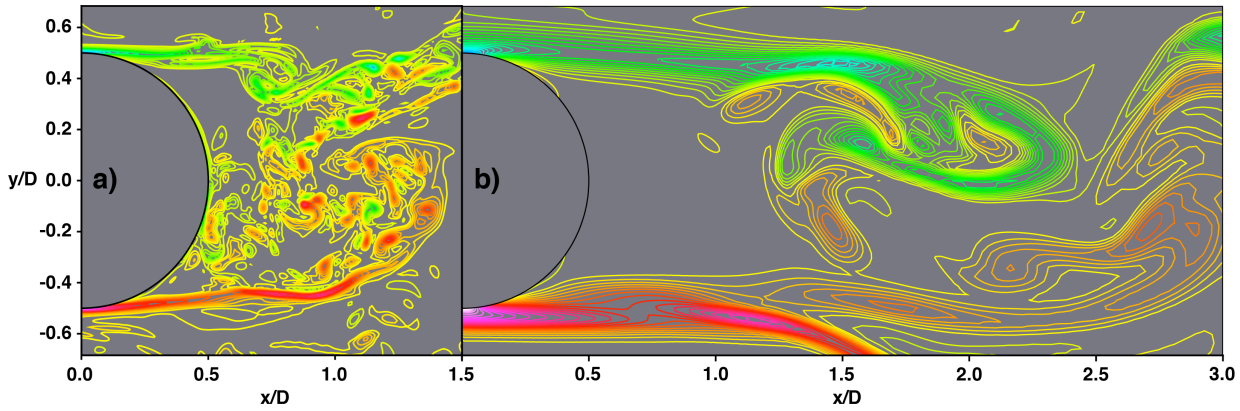

Fig. 8. Instantaneous contours of spanwise vorticity in an (x, y) plane, a) Case A (n = 470, k = 1) and b) Case E (n = 2560, k = 1).

Contours of time-averaged spanwise vorticity for the cases A and E are provided in Figs.10a and 10b, respectively. These figures clearly show the much larger separation between the upper and lower shear layers in Case A compared to that obtained in Case E. The proximity of the two shear layers, assuming that the thickness of the shear layers remains approximately same, can be expected to have a significant effect on the shed vortex formation process. This effect of decreasing separation distance will become more apparent in Case F that is discussed in the next section. A second feature of interest in Fig. 10 is the streamwise extent of the high vorticity region; it is about twice as much in Case E, in terms of the diameter D, as in Case A. The minimum and maximum values of spanwise vorticity and the number of contours plotted is identical in Figures 8, 9 & 10.

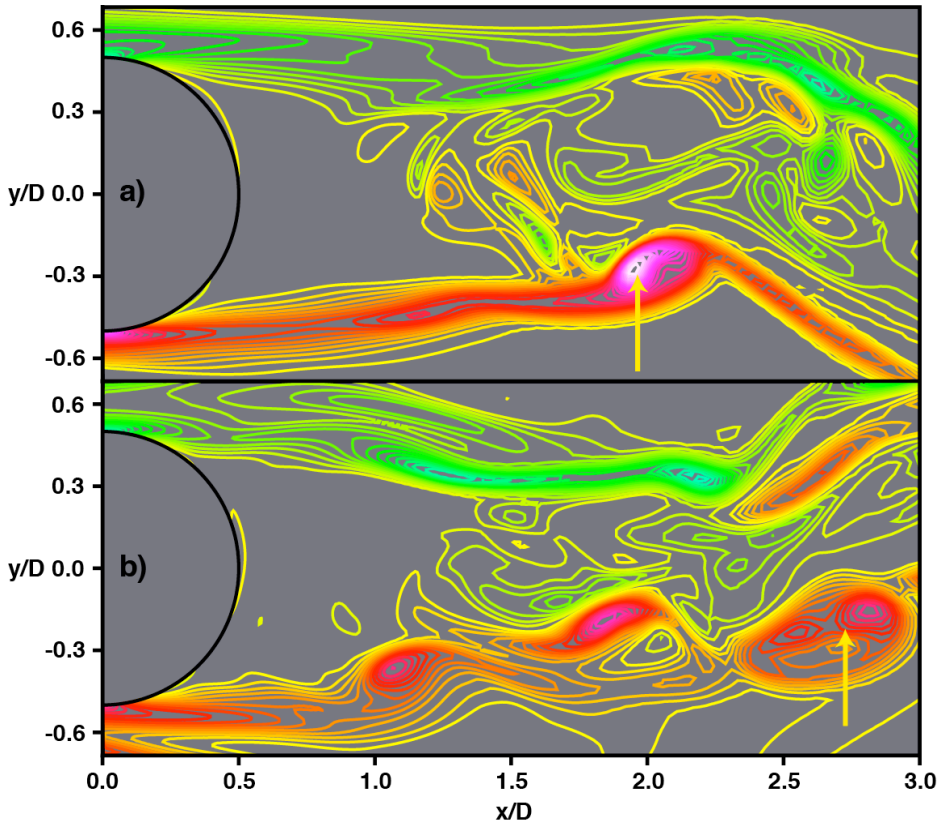

Fig. 9. Instantaneous contours of spanwise vorticity in an (x, y) plane, Case E (n = 3000), a) z/D = 0.0, b) z/D = 4.0 (midspan).

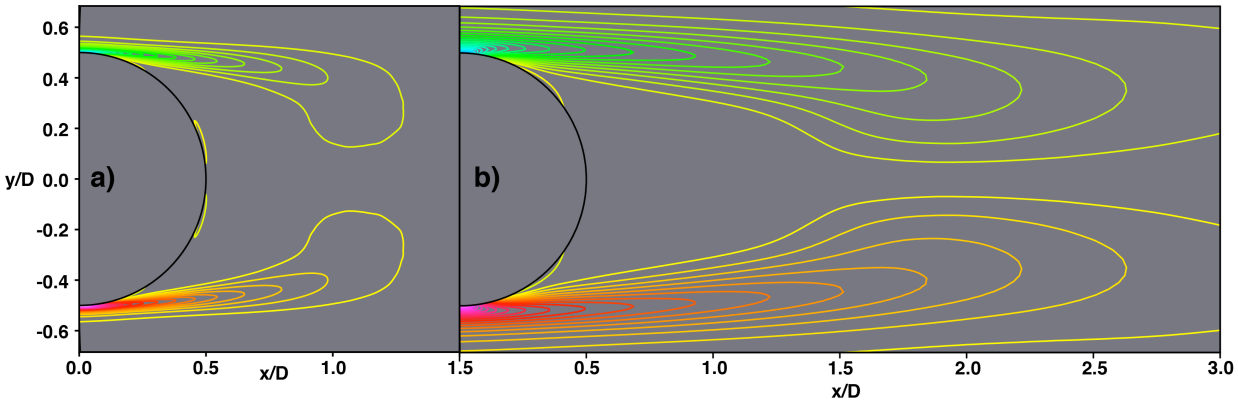

Fig. 10. Time-averaged contours of spanwise vorticity in an (x, y) plane, a) Case A b) Case E.

Earlier, in the case of the cylinder, the circulating flow associated with an incipient shed vortex was a result of reverse flow very near and tangential to the base (below the centerline) caused by an earlier shed vortex (positive), the reverse and upward flow (below the centerline) induced by the recently formed negative vortex that moves downward and to the right (going from phase ϕ_A to ϕ_B), and the forward flow in the lower shear layer and further below. It is of interest to determine if the same or a similar process exists in the wake of the flat plate with turbulent separating boundary layers in the case with more conventional shedding, Case A. Because of the highly disturbed nature of the base flow (containing recirculation region vortices, shear layer instabilities etc., see for example Fig. 8a), we use the phase-averaged velocity and pressure fields instead of their instantaneous versions. Details regarding

the phase-averaging method are provided in Rai (2013). The phase $\phi = 0.0$ ($0.0 \leq \phi \leq 1.0$) corresponds to the phase when the center of the upper shed-vortex is at x/D = 5.5.

Figure 11 shows phase-averaged velocity vectors and pressure contours at the phase $\phi = 0.24$. The location of the center of the upper shed vortex is evident.

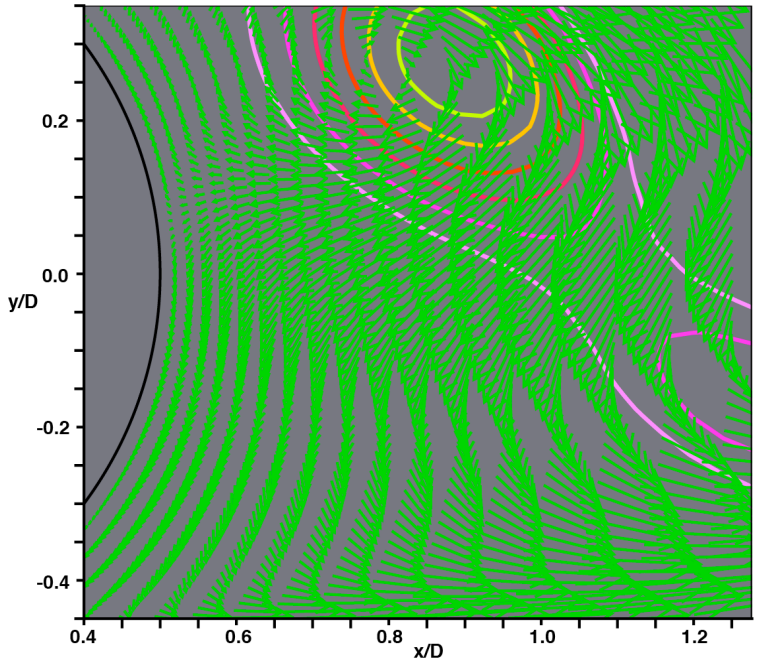

Fig. 11. Phase-averaged velocity vectors and pressure contours, Case A, $\phi = 0.24$ (vectors constructed only at 5% of the grid points).

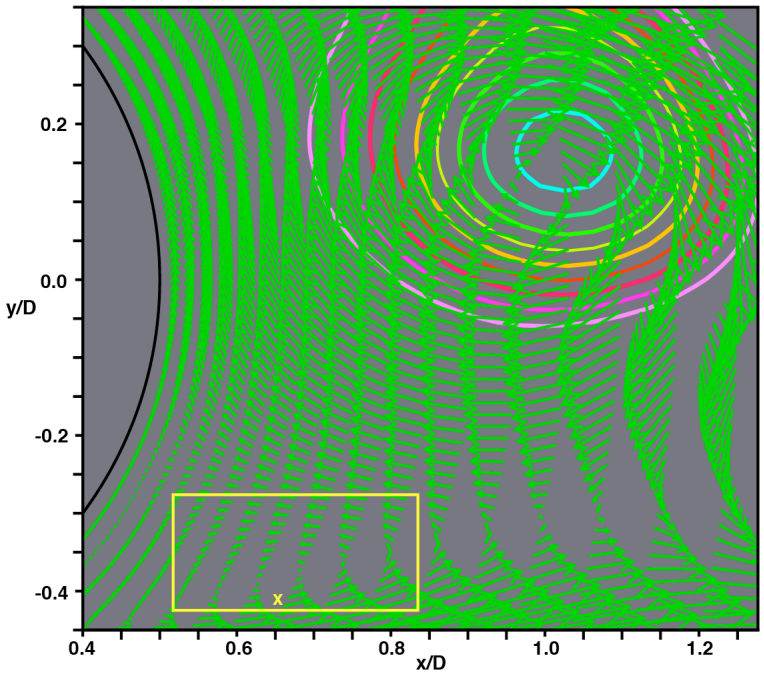

Fig. 12. Phase-averaged velocity vectors and pressure contours, Case A, $\phi = 0.44$ (vectors constructed only at 5% of the grid points, point X located at x/D = 0.65, y/D = -0.41).

As in Fig. 1a for the cylinder, the flow below the wake centerline moves downward and then turns sharply to the right. Circulating flow below the wake centerline is absent at this phase. Figure 12 shows phase-averaged velocity vectors and pressure contours shortly thereafter at ϕ = 0.44. As in Fig. 2a for the cylinder, the upper shed vortex has moved downward and to the right, and causes flow reversal below the centerline. The flow in the shear layer region is to the right and upward. The flow very near the base continues to be downward (remnant of the flow induced by the previous positive shed vortex). Again we have the essentials for circulating flow. The result is the region of circulating flow within the rectangle. The symbol x marks the pressure minimum. Figures 1 - 3 and Figs. 11 – 12 indicate that the shedding process in Case A, in a phase-averaged sense, is similar to that of the cylinder.

Figure 13 shows phase-averaged spanwise vorticity contours at vortex initiation, ϕ = 0.44, and at a later phase, ϕ = 0.68. The pressure minimum initially occurs near the inner edge of the lower shear layer (marked with an x in Fig. 13a). Shear layer roll-up is minimal at this phase. In Fig. 13b, circulatory flow induced by the newly formed vortex causes a redistribution of the shear layer vorticity that results in the bulbous appearance of the lower shear layer. A peak in vorticity is not yet apparent. The pressure minimum (again marked with an “x”) has moved to the right and toward the centerline. The more mature positive vortex in Fig. 13a (which can be considered the evolved version of the newly formed vortex but at the phase ϕ = 1.44) exhibits the expected peak in vorticity. The pressure peak associated with this vortex (marked with an “o”) is almost coincident with the peak in vorticity.

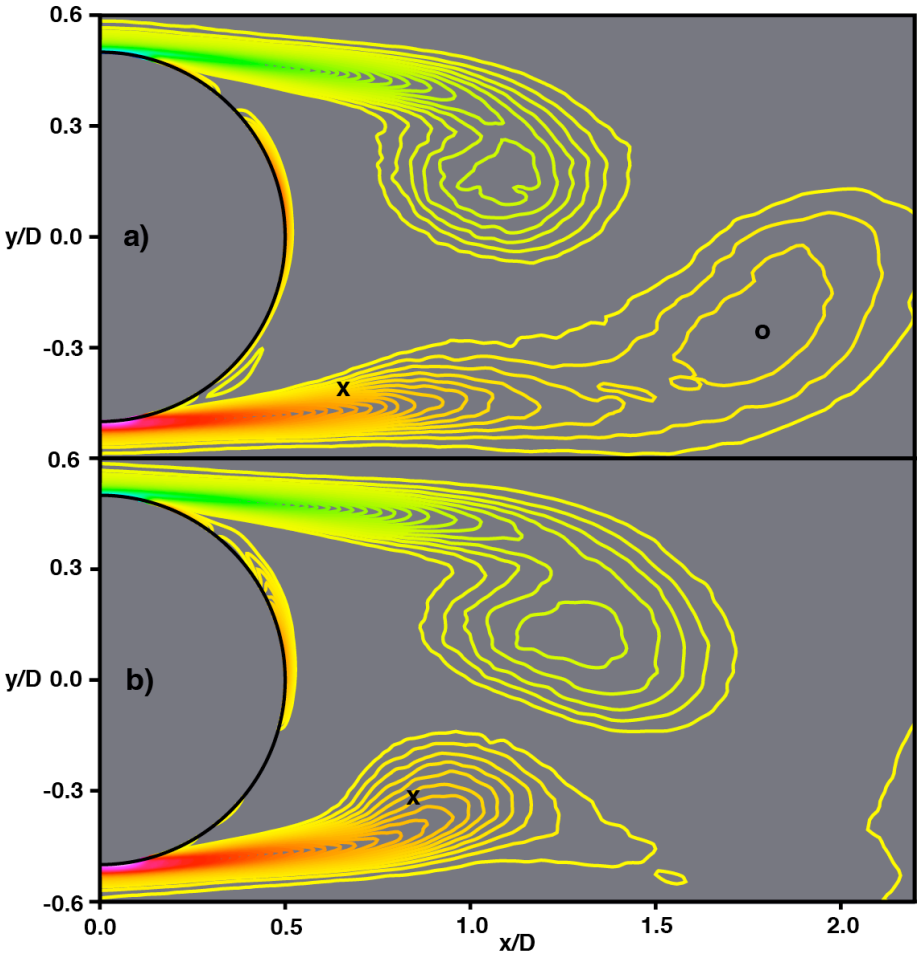

Fig. 13. Phase-averaged spanwise vorticity for Case A at a) ϕ = 0.44 and b) ϕ = 0.68.

Flow Visualization for Case F

The reductions in Re_D in cases D and E in comparison to Case A resulted in the start of deterioration in the shedding process. We now focus on Case F where Re_D is a quarter of that of Case E while Re_θ is nearly the same ($Re_{D,E} = 4.0Re_{D,F}$ & $Re_{D,A} = 16.0Re_{D,F}$). The shedding characteristics obtained in Case F are significantly different and are discussed below. As in Case E, the physical spanwise dimension in Case F is the same as in Case D. This results in the spanwise dimension in Case F being 32.0D.

A top view of instantaneous surfaces of constant negative λ_2 (λ_2 being the second eigenvalue of $\boldsymbol{S}^2 + \boldsymbol{\Omega}^2$, see Jeong & Hussain, 1985) in the region -1.0 < y/D < 1.0, for Case F are provided in Fig. 14. While surfaces of constant pressure also show similar features, surfaces of constant negative λ_2 more clearly depict the vortices in this case. The vorticity field in Case F is considerably different than that obtained in Cases A, D & E (Figs. 6a, 6b & 6c). Sequences of nearly spanwise vortices, between 1.0D & 4.0D in length, are evident. Some of the sequences are marked with arrows. While two of the marked sequences show vortices well aligned with the z direction, one of them occurs at an angle of approximately 30°. Some of the vortices are even aligned with the x direction and are probably streamwise vortices from the upstream boundary layers.

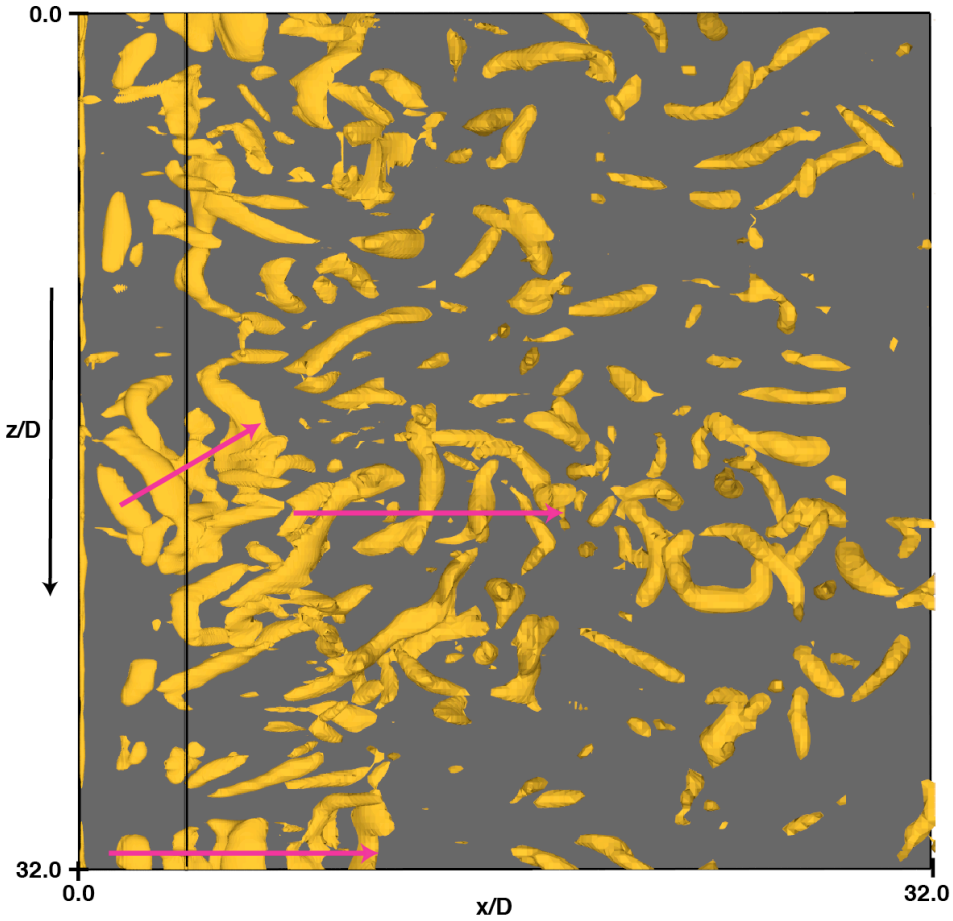

Fig. 14. Instantaneous surfaces of constant λ_2 (negative) in the region -1.0 < y/D < 1.0, Case F, (top view, n = 200,000).

The two most significant features of Fig. 14 are a) the spanwise vortices are of finite length in the z direction and b) the sequences are also finite. If indeed the sequences comprise shed vortices, then

shedding seems to be intermittent in Case F. Some of the questions that Fig. 14 raises are as follows: Are the spanwise vortices shed vortices? If so, is the shedding process similar to the more conventional shedding of Cases A & D? What is the cause of intermittency in shedding? What causes the shed vortices to be of finite length? How does the spectrum obtained for the cross-stream velocity in Case F compare with that of Case D at the wake centerplane? Does the spectrum have a sharp peak? How do the fluctuations in velocity magnitude compare in the two cases? In the following we provide some of the answers to these questions.

Figure 15 shows contours of instantaneous spanwise vorticity at z/D = 0.0 and at the same time instant as in Fig. 14. Firstly we see the upper and lower detached shear layers have nearly merged very close to the trailing edge, hence the separation distance between the two, that was discussed with regard to the earlier cases, is essentially non-existent. There is very little room for a traditional shear-layer roll-up, given the thickness of the detached shear layers in relation to the diameter of the trailing edge. Instead we have here, shed vortices (positive ones marked with blue arrows and negative ones with red arrows) that are essentially confined to the shear layers for about the first fifteen diameters (it will become evident shortly that these are indeed shed vortices). Beyond 20 diameters the shear layers breakdown but the vortices persist. The vortices seen in the first 12 diameters are also seen in Fig. 14 (the sequence closest to the lower and upper boundaries in the figure). Although a conventional roll-up is largely prevented by the proximity of the shear layers, the shed vortices, because of their combined induced velocity field, result in shear layers that are sinuous in appearance. Also evident in Fig. 15 are the log-layer eddies from the upstream boundary layers, further removed from the centerline, convecting downstream. Clearly, shedding in Case F is significantly different than in Cases A & D.

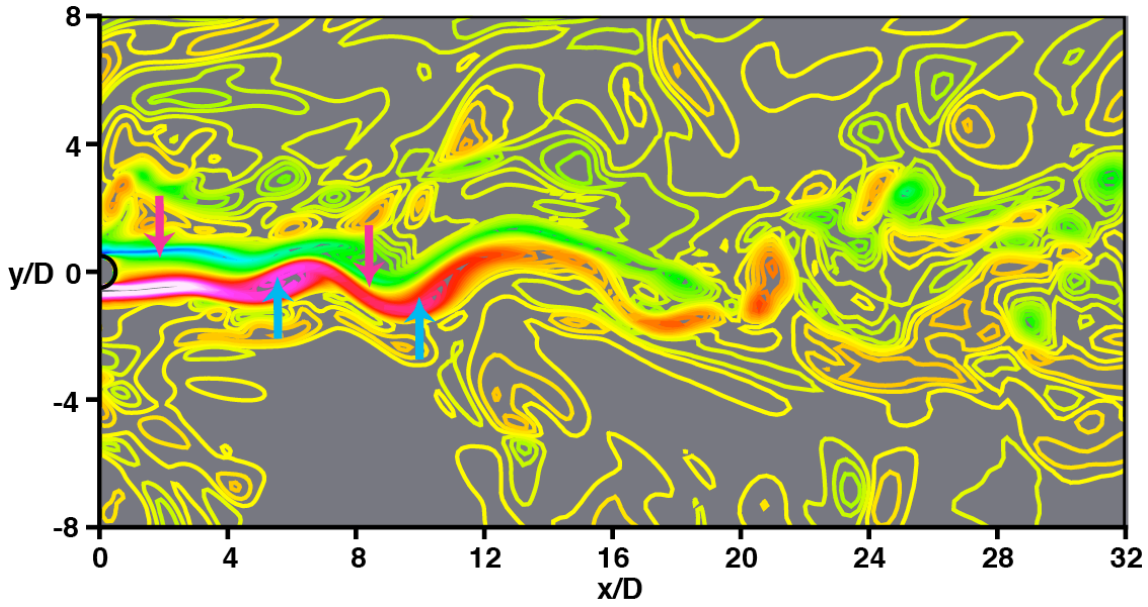

Fig. 15. Instantaneous contours of spanwise vorticity in a (x, y) plane, Case F (z/D = 0.0, n = 200,000).

Shed vortices close to the wake centerplane result in cross-stream flow at this plane. We have downwash between a negative/positive shed vortex pair (vortices occurring in that order in the streamwise direction) and upwash between a positive/negative vortex pair. Figure 16 shows contours of cross-stream velocity *v* over 20 shedding cycles in the (t, z) plane for Case D at x/D = 4.0. The figure shows bands that are nearly vertical, and significant small-scale activity. As expected, the bands are similar to the ones seen in Fig. 7b around x/D = 4.0 (which shows contours of instantaneous *v* in the wake in the *(x, z)* plane for Case D).

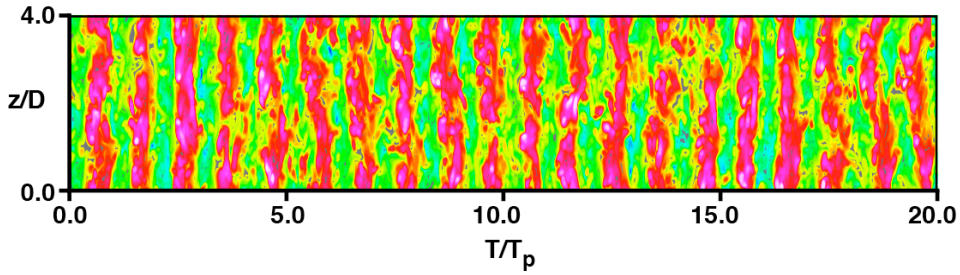

Fig. 16. Contours of cross-stream velocity at x/D = 4.0, y/D = 0.0 over 20 shedding periods (Case D).

Figure 17 shows *v* over 20 shedding cycles in the (t, z) plane for Case F at x/D = 4.0. Only half of the spanwise extent of the computational domain is included in this figure, and contours corresponding to values of *v* close to zero have been omitted for clarity. The features discussed earlier with regard to Fig. 14 are also evident here. The bands on average are between one and four diameters in length. They occur in sequences whose lifetimes vary and consist of pairs of opposing color (upwash/downwash). While most bands are nearly vertical, some of them occur at noticeable angles to the vertical. The differences between Figs. 16 & 17 are striking.

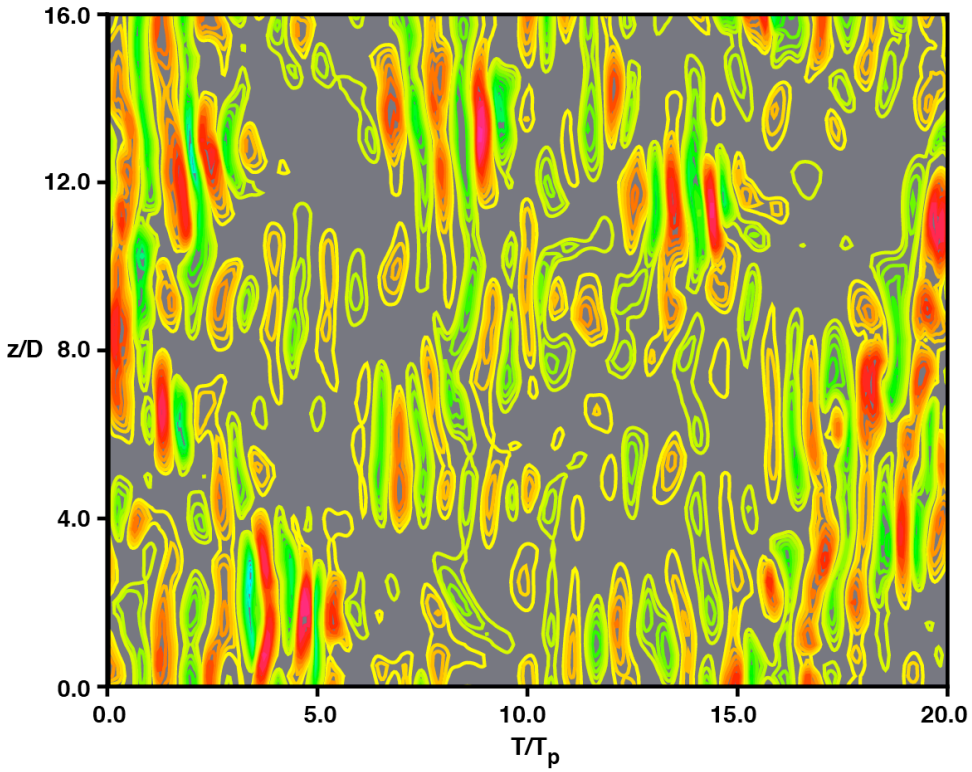

Fig. 17. Contours of cross-stream velocity at x/D = 4.0, y/D = 0.0 over 20 shedding periods (Case F).

While the bands in Fig. 17 show the relation between the shed vortices of Fig. 14 and upwash/downwash in the centerplane, the spaces between the sequences of bands (inter-sequence spaces) are of equal importance. The spaces that occur between sequences (in the T direction) may provide insight into intermittency. For example, why do sequences weaken and taper off? Similarly, spaces between sequences in the z direction may shed light on the reasons underlying the finite length of the bands (and associated shed vortices). Potential inter-sequence spaces for further study were selected by first plotting a large number of contours but with the same minimum/maximum values of *v* as in Fig. 17 and then picking those regions with very few or no contours. It was determined via (x, y) plots of instantaneous spanwise vorticity, in the regions thus selected, that occasionally shed vortices of nominal

strength were present but the detached shear-layer in which they were embedded was displaced significantly from the centerplane because of large fluctuations in the separating boundary layer. The displacements are sufficiently large to cause a significant weakening of upwash/downwash at the centerplane. The shed vortices during these periods can be visualized by choosing a larger range of y in Fig. 14. However, at other times the detached shear layers become relatively quiescent and the instability manifests very weakly. It is possible that the disturbances present in the separating boundary layer interfere with the shed-vortex formation process. The nature of this interference is yet to be determined.

Figure 18 shows spectra for fluctuating *v* at x/D = 4.0 on the wake centerline for cases D & F. Both of them show a peak at shedding frequency ω_{st}. However, Case D exhibits a sharp peak whereas in Case F the peak is wide, thus indicating larger fluctuations in shedding periods in the latter case. The ratio in peak values (D to F) is 17.2. Hence there is a substantial reduction in upwash/downwash caused by the shed vortices with increasing θ/D. The shed vortices in Case F are considerably weaker than those of Case D thus resulting in significantly lower cross-stream velocities and corresponding peak in the fluctuating *v* spectrum. In addition, the shed vortices in Case F appear intermittently and are of finite length, and this results in further reducing the peak value. The decrease in fluctuating *v* is discussed in more detail in the next section comprising velocity statistics in the wake.

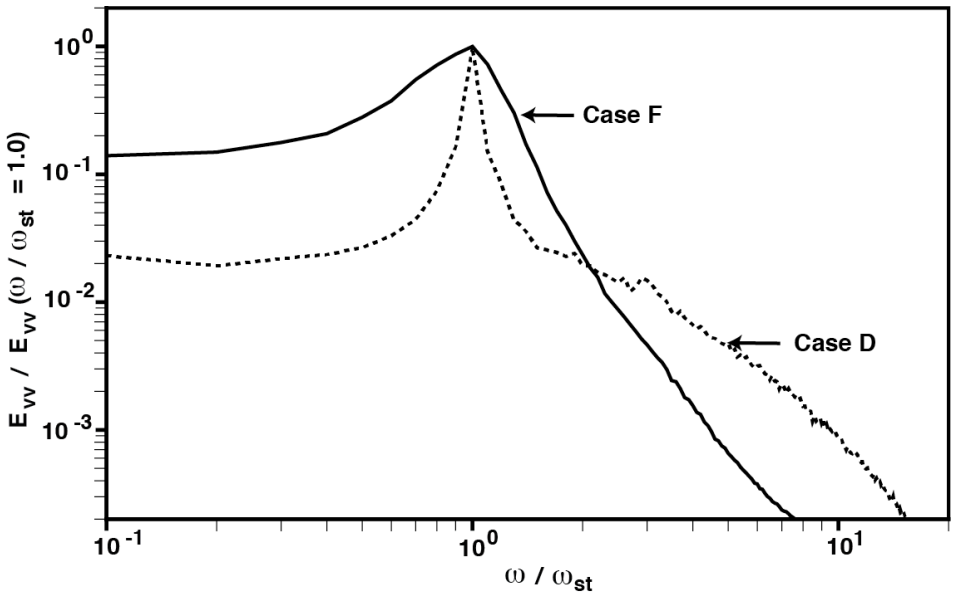

Fig. 18. Comparison of spectra obtained for fluctuating *v* in Cases D & F, x/D = 4.0.

Earlier, in Figs 11 & 12, the shedding process in Case A was investigated with the aid of phase-averaged velocity vectors and pressure contours. The process was found to be quite similar to that encountered in the case of the cylinder. Here again, in Case F, with all its complexity (intermittent shedding, shed vortices that are finite in length and for several diameters of travel are confined to the shear layer etc.) one would like to ascertain if there are differences in the initial causes for circulating flow. Figures 19 and 20 show velocity vectors and pressure contours at two instants in time (separated by a fraction of the shedding period). These figures are counterparts of Figs. 11 & 12, respectively, except for the fact that instantaneous flow variables are used instead of phase-averaged variables (the more quiescent base region, absent recirculation region vortices etc. makes this possible). Once again the essential component for circulatory flow below the centerline appears with the downstream movement of the upper shed vortex (the reverse flow this movement causes just below the centerline). The downward flow very near the base (below the centerline) is a remnant of the flow induced by the previous positive shed vortex, and the forward flow in the lower shear layer region is present as well. As a result we obtain the circulating flow within the region contained by the rectangle. This process was observed repeatedly. Clearly, the shedding process in Case F is also quite similar to that found in the case of the cylinder.

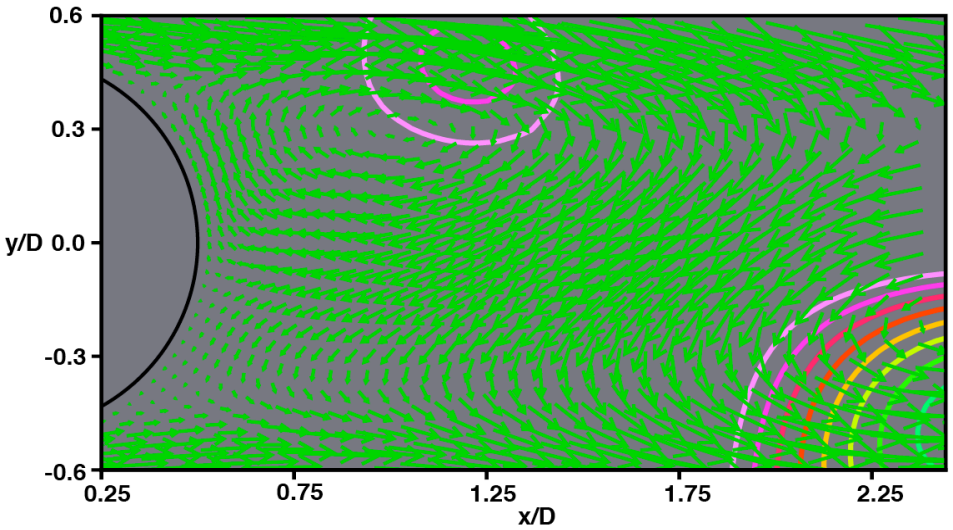

Fig. 19. Instantaneous velocity vectors and pressure contours, Case F (z/D = 0.0, n = 180,280).

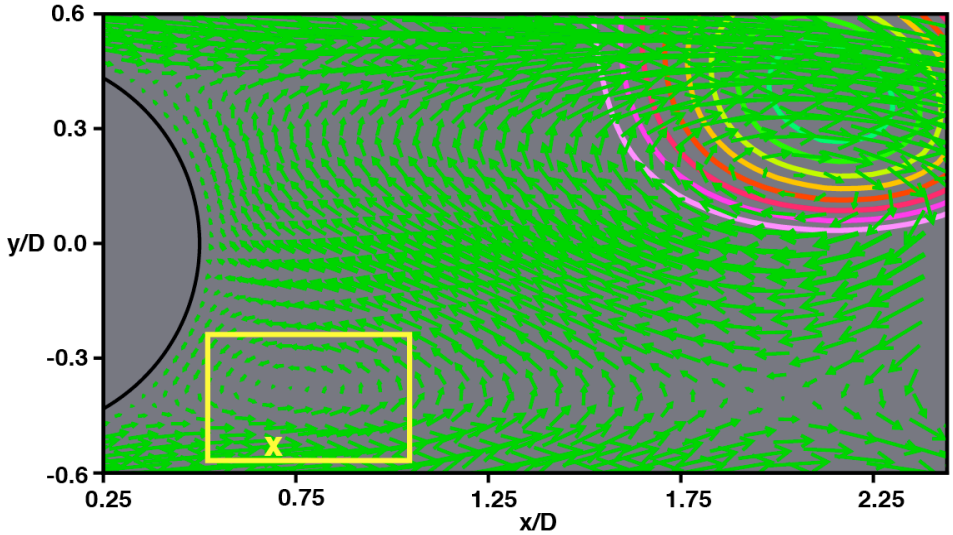

Fig. 20. Instantaneous velocity vectors and pressure contours, Case F (z/D =0.0, n = 180,440).

Time-Averaged Velocity Statistics in the Wake for Cases D & F

The distribution of time-averaged velocity statistics (also averaged in the z direction) in the wake region for Cases D and F are presented in this section. Earlier investigations by the present author (Rai 2013 & 2014) have included phase-averaged velocity statistics. Clearly this is difficult (for reasons discussed earlier) and also of limited utility in Case F. Distributions of time-averaged values of velocity components and spanwise vorticity are presented first followed by distributions of time-averaged fluctuating kinetic energy and shear stress. Fluctuations include those due to quasi-periodic shedding and the random component. *The minimum and maximum values and the numbers of contours in the subplots in the following figures are identical; the subplots within a given figure may be directly compared.*

Figures 21a and 21b provide contours of time-averaged streamwise velocity u for Cases F & D, respectively. The dashed white line corresponds to $u = 0.0$; thus the region between the base and this line consists of reverse flow. The separated region obtained in Case F is significantly larger in size although separation occurs sooner on the trailing edge surface in Case D. The zero contour line crosses the

centerline at 1.87D and 3.12D for cases D and F, respectively. Thus the ratio of the lengths of separation in the two cases is 0.52 (D to F, (1.87 - 0.50)/(3.12 - 0.50)). Peak reverse flow occurs at 1.41D and 1.77D for cases D and F, and the ratio of peak negative u values in the two cases is 2.73 (D to F). As expected reverse flow in Case F is much weaker. The color palette indicates a more rapid recovery of streamwise velocity past the $u = 0.0$ contour line both in the x and y directions in Case D.

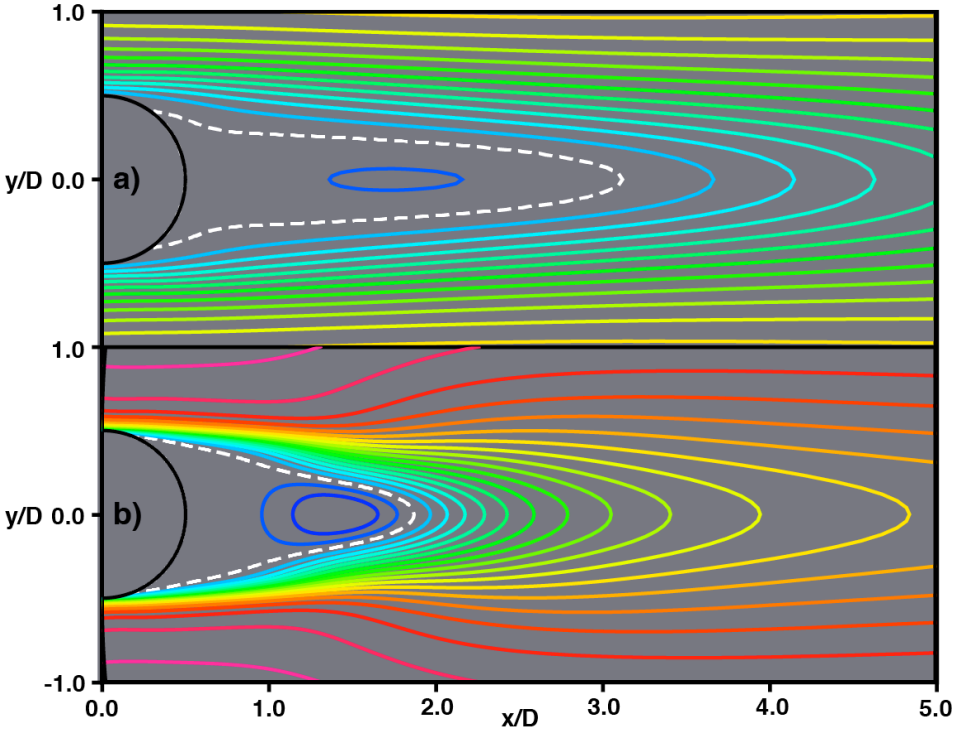

Fig. 21. Contours of time-averaged streamwise velocity, a) Case F, b) Case D.

Contours of time-averaged cross-stream velocity for Cases F and D are shown in Figs. 22a and 22b, respectively. In Figure 22b we see a positive peak in the upper half of the plane at x/D = 1.07 and a negative one at x/D = 1.74. These peaks indicate the reverse flow in the base region and the induced cross-stream flow caused by the negative shed vortices, respectively. The lower half shows a reflection of the contours seen in the upper half (with a sign change). The data obtained in Case F (Fig. 22a) are qualitatively similar but the cross-stream flow is considerably weaker. The positive peak in the upper half of the plane occurs close to the base and is associated with the reverse flow in this region. The negative peak, however, is relatively quite distant from the base; it occurs at 3.74D. Centerline cross-stream intensity level at a given streamwise location and average shed-vortex strength at the same location are directly related (through the upwash/downwash at the centerline resulting from the passage of the shed vortices). As will be seen shortly, the centerline cross-stream intensity level peaks at about 8.14D in Case F (although there is little variance of this quantity between 6.0D and 10.0D). In Case D the peak occurs at 2.09D. Thus peak shed-vortex strength occurs much further downstream in Case F compared to Case D. Correspondingly, the peak in negative cross-steam velocity (in the upper half of the plane) also occurs at a larger value of x/D. A discussion of the effect of increasing Re_θ and decreasing Re_D (both of which occur going from Case D to Case F) on phase-averaged vortex strength, cross-stream velocity and assimilation/entrainment for Cases A, C & D is provided in Rai (2015).

Figures 23a and 23b show contours of time-averaged spanwise vorticity for Cases F and D, respectively. Contours corresponding to vorticity values close to zero have been omitted in Fig. 23. The DSLs and the corresponding regions of higher vorticity are seen located substantially away from the centerline and only for x/D < 2.0 in Case D. In Case F the DSLs extend beyond x/D = 5.0. In addition

there is little separation between the two DSLs from about x/D = 1.0 onwards in Case F, thus indicating the strong interaction between them and the difficulty in a shear-layer roll-up that accompanies the conventional shed-vortex formation process.

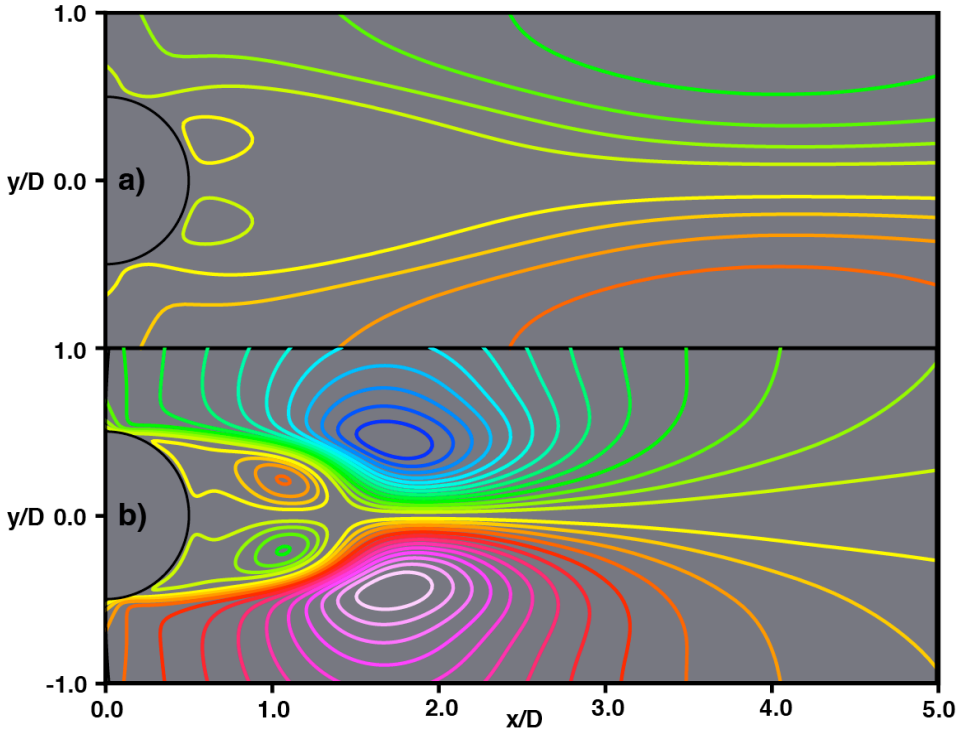

Fig. 22. Contours of time-averaged cross-stream velocity, a) Case F, b) Case D.

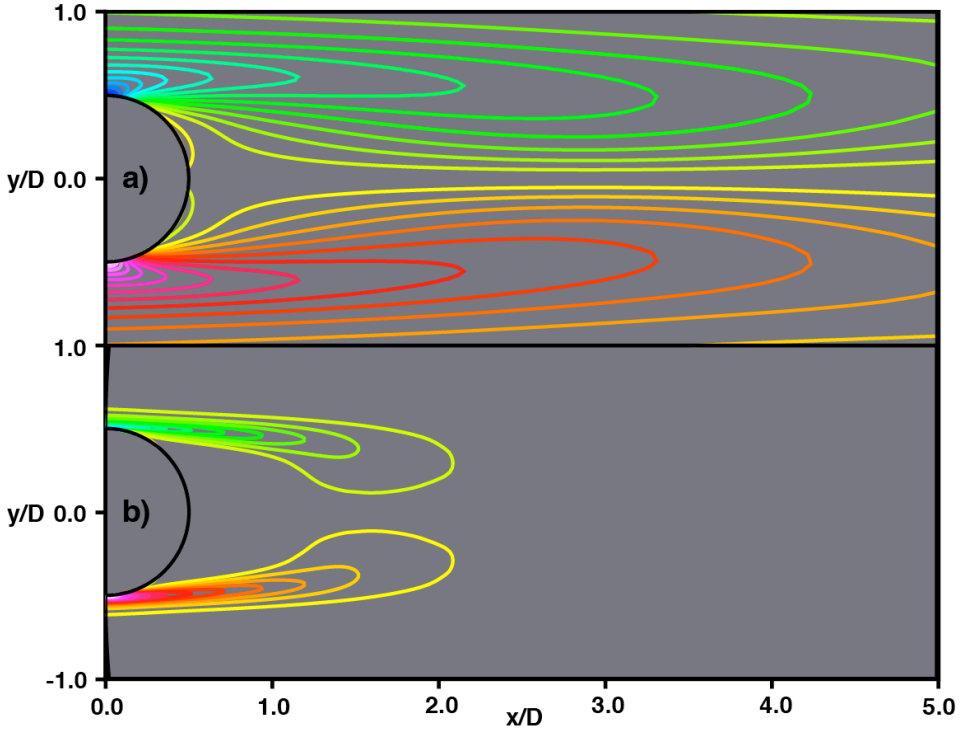

Fig. 23. Contours of time-averaged spanwise vorticity, a) Case F, b) Case D.

We now turn our attention to distributions of fluctuating intensity and shear stress in Cases D and F. Figure 24 shows the variation of streamwise and cross-stream intensities with x/D along the centerline for the two cases. While peak values of streamwise intensity are roughly the same (Case D shows a slightly larger peak), peak cross-stream intensity levels are substantially different. The peak value in Case D is 6.64 times larger and occurs closer to the base. The reason for this has been alluded to earlier (weaker shed vortices in Case F that reach their peak strength further downstream). A second difference between the two cases is that while the peak in cross-stream intensity is higher than the peak in streamwise intensity in Case D, the reverse is true in Case F. The primary cause for the reversal in trend is again the relative weakness of the shed vortices in Case F that results in significantly diminished cross-steam intensity levels. While the streamwise intensity level is also somewhat diminished in Case F, much of it is inherited from the boundary layer and therefore it is not affected to the same extent.

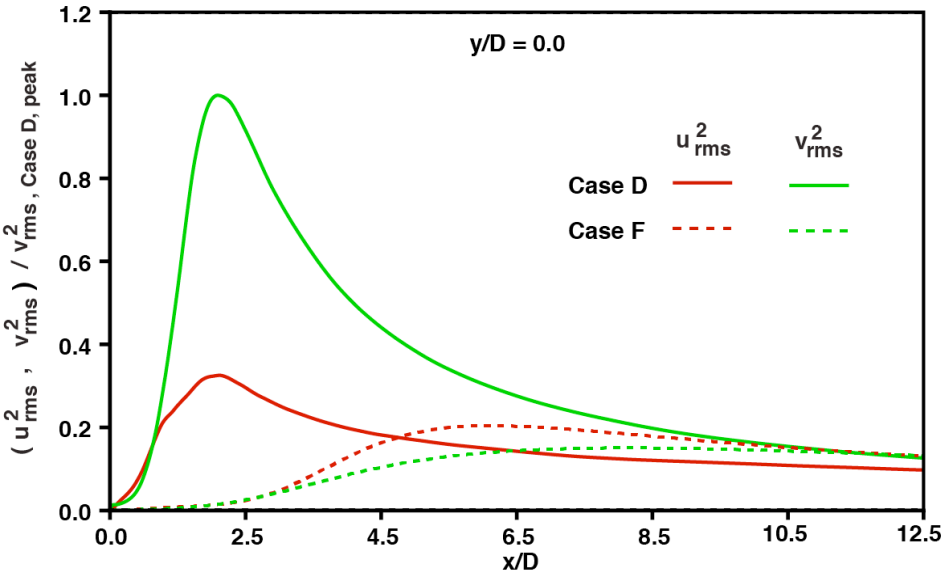

Fig. 24. Variation of streamwise and cross-stream intensities along the wake centerline for Cases D & F.

Figures 25a and 25b show contours of time-averaged fluctuating kinetic energy (all three-components, including both random and quasi-periodic fluctuations). While they are topologically similar, feature scales and locations are substantially different, again, because the region in which shed vortices are strongest is further downstream in Case F when compared to Case D. As expected both figures show non-zero levels in the turbulent separating boundary layers. A peak in intensity is observed in both cases. However, the peak in Case D is higher (stronger shed vortices) and occurs closer to the base (3.69 times higher and located at x/D = 2.00 instead of 5.93 as in Case F). In addition, peak values in Case D, unlike Case F, occur very close to the centerline. This is because shed vortices in Case D are still in the final stage of formation at x/D = 2.0 and are close to the centerline. In contrast, as seen in Fig. 15, the sinuous behavior of the shear layers in Case F, their relative thickness in relation to plate thickness and the fact that shed vortices are confined to the shear layer for several diameters downstream of the base all contribute to the shed vortices being further away from the centerline than in Case D.

Contours of time-averaged fluctuating shear stress for Cases F and D are provided in Figs. 26a and 26b, respectively. The primary peak values (negative above and positive below) are seen in both cases. The locations roughly correspond to the locations of the peaks in Figs. 25a and 25b. The peak levels obtained in Case D are higher. The reasons for these two attributes are the same as those provided for Figs. 25a and 25b. In addition to the primary peak in Fig. 26b, there exist much weaker secondary peaks (opposite in sign to primary peaks) close to the base (see arrows). The secondary peaks are present even for Case F but are much too weak to be seen even with the large number of contours used in Figs. 26a and 26b. The origin of the secondary peaks is discussed at length in Rai

(2011). It is shown there, in the context of Case A, that they are caused by the *periodic component* of fluctuating velocities (u & v) resulting from the formation of the shed vortices. These two velocity components are found to be positively/negatively correlated in the vicinity of the upper/lower secondary peak. Time-averaged velocity statistics for the periodic and random components and the sum of the two (total value) for Case A are provided in Rai (2011). The secondary peaks were also obtained experimentally and computationally in Dong et al (2006) for a cylinder at Re_D = 10,000 (laminar boundary layers, total value of fluctuating shear stress).

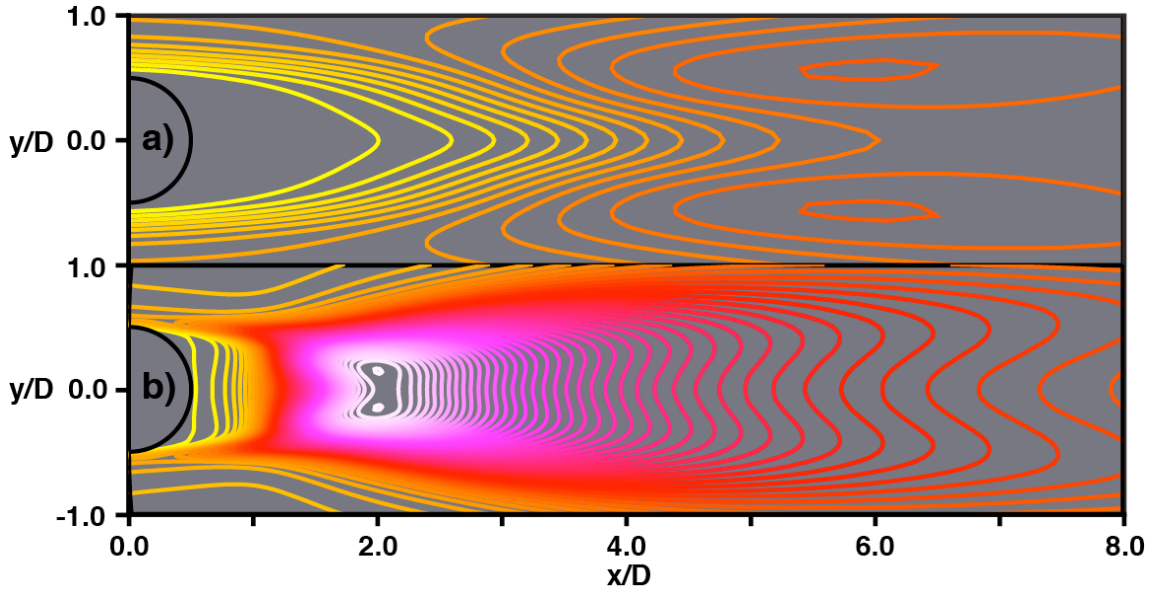

Fig. 25. Contours of time-averaged fluctuating kinetic energy, a) Case F, b) Case D.

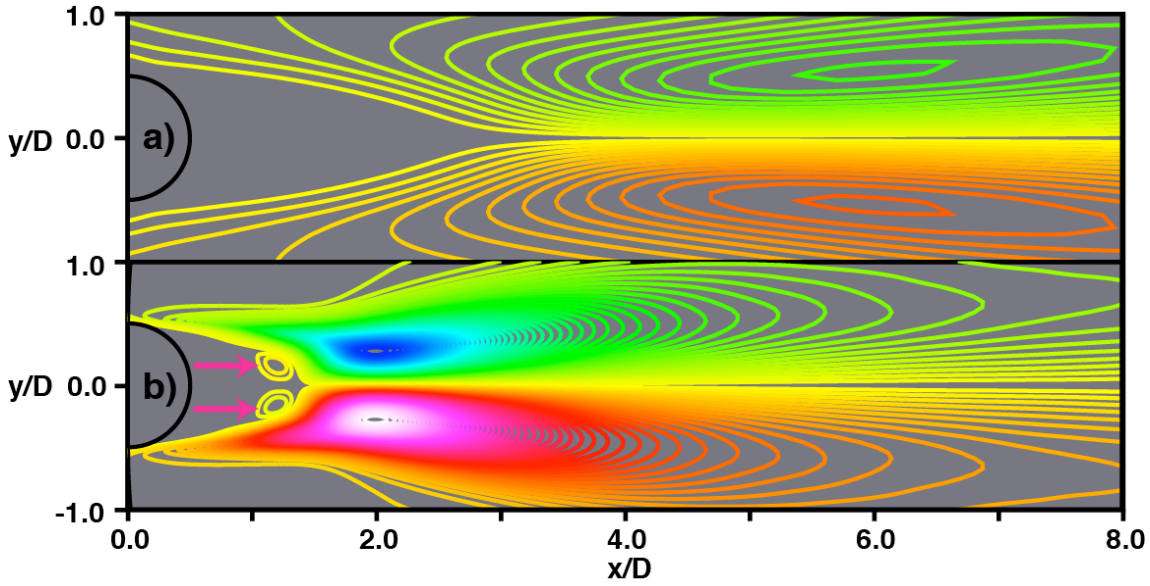

Fig. 26. Contours of time-averaged fluctuating shear stress, a) Case F, b) Case D.

A Functional Relationship Between Shedding Frequency and Re_θ & Re_D

The range of Reynolds numbers (Re_θ and Re_D) covered by Cases A - F is substantial and permits the development of various correlations (between the quantity of interest and these two Reynolds numbers). A power-law relationship between the ratio of shear-layer frequency to shedding frequency and Re_θ and Re_D was developed in Rai (2015) using just the Cases A – D. Cases A – C were used to obtain the necessary exponents and constant. The power-law was then used to predict the frequency ratio for Case D. The predicted and computed (via DNS) frequency ratios were very close, 2.57 and 2.58, respectively. The proximity of these two values was obtained even though the power-law was used in an extrapolative mode to predict the frequency ratio for Case D (Cases A – D are at the vertices of a rectangle in Re_L – Re_D space). A second power-law relationship between the normalized, phase-averaged, peak spanwise vorticity at shed vortex cores when they are located at x/D = 5.5 was also developed in Rai (2015) using Cases A - C. The estimated and computed spanwise vorticity values for Case D differed by about 10%. Here again, the power-law was used in an extrapolative mode. Although the estimate is not as accurate as that obtained for the frequency ratio, it is quite reasonable.

Here we obtain a functional relationship between the shedding frequency (ω) and Re_θ and Re_D. An initial interrogation of the data revealed a relatively weak dependence of ω on Re_θ (ω decreased with increasing Re_θ at constant Re_D). Cases A, D, E & F (all with the same plate length) showed only a relatively small variation of Re_θ. Hence, the variation of ω with Re_D was investigated for these four cases (assuming the effect of Re_θ was negligible). It was determined via this exercise that $1/\omega$ showed a nearly linear variation with Re_D. Hence, the following proportionalities were assumed (P & Q are constants):

$$1/\omega \propto \mathrm{Re}_\theta^{\alpha}$$
$$1/\omega \propto (P + Q\mathrm{Re}_D^{\beta}) \qquad (1)$$

The above expressions result in the following functional relationship between ω and Re_θ and Re_D.

$$(\omega_A/\omega)\,((\mathrm{Re}_\theta)_A/\mathrm{Re}_\theta)^{\alpha} = \mathrm{A} + \mathrm{B}\,(\mathrm{Re}_\mathrm{D}/(\mathrm{Re}_\mathrm{D})_A)^{\beta} \qquad (2)$$

In Eq. 2, A and B are constants (with the constraint A + B = 1), the subscript A refers to Case A and Re_θ is computed at x/D = 0.0 (very close to the location of boundary layer separation). Alternatively, Eq. 2 can be written as

$$((\omega_A/\omega)\,((\mathrm{Re}_\theta)_A/\mathrm{Re}_\theta)^{\alpha} - \mathrm{A})/\mathrm{B} = (\mathrm{Re}_\mathrm{D}/(\mathrm{Re}_\mathrm{D})_A)^{\beta} \qquad (3)$$

The constants A and B and the exponents α and β were all obtained from a least squares fit to the computed data for Cases A – F. The values of α and β thus obtained are 0.1156 and 1.1520, respectively. The value of α is small and nearly an order of magnitude smaller than that of β. Clearly, variations in Re_D result in more significant changes in ω than similar variations in Re_θ. In addition, the value of β is close to unity, showing a nearly linear relationship between $1/\omega$ and Re_D.

Figure 27 shows a plot of the variable

$$((\omega_A/\omega)\,((\mathrm{Re}_\theta)_A/\mathrm{Re}_\theta)^{\alpha} - \mathrm{A})/\mathrm{B}$$

(LHS of Eq. 3) for each of the six cases (values of ω and Re_θ obtained from the direct numerical simulations) as a function of $(Re_D / (Re_D)_A)$. Figure 27 also shows a plot of the function $(Re_D / (Re_D)_A)^{\beta}$. The computed data (symbols) and the curve are close, thus indicating the validity of the model of Eq. 2

(and the computed constants and exponents) for the range of Reynolds numbers investigated here (a factor of 16 in Re_D and about 5 in Re_θ).

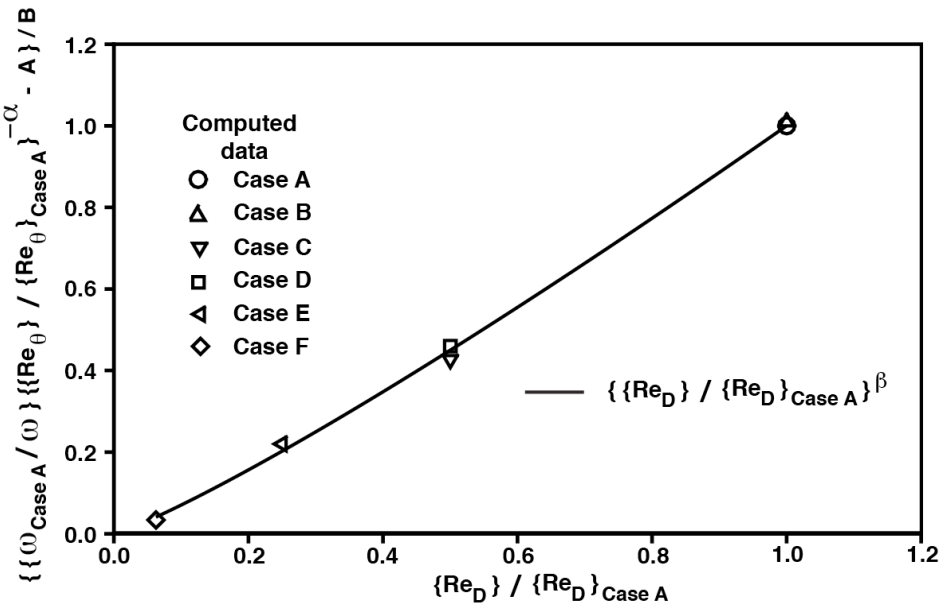

Figure 27. A test of the proposed model relating ω and Re_θ & Re_D (Eq. 3), using the DNS data and estimated constants/exponents.

CONCLUDING REMARKS

The very near and near wake of a flat plate with a circular trailing edge is investigated with data from direct numerical simulations. Computations were performed for six different combinations of the Reynolds numbers based on plate thickness (D) and boundary layer momentum thickness upstream of the trailing edge (θ). The separating boundary layers are turbulent in all the cases investigated. One objective of the study was to understand the changes in the wake vortex shedding process as the plate thickness was reduced (increasing θ/D). The value of D varies by a factor of 16 and that of θ by approximately 5 in the computations. The second objective was to understand the effect of changing these two parameters on near wake velocity statistics.

The direct numerical simulations of the flat plate wakes show that vortex shedding is vigorous in the low θ/D cases (Cases A and D) and that there is a substantial decrease in shedding intensity as θ/D increases (Cases E & F). In addition a lack of coherence in the spanwise structure of the shed vortices was observed with increasing θ/D. An important finding of the present study (using Cases A, D, E & F) is that the interaction between the upper and lower shear layers becomes stronger as D is decreased (keeping θ approximately the same). Also, the proximity of the shear layers (relative to θ) in the large θ/D cases, essentially reduces the ability of the shear layer to roll-up and contribute to the strength of the newly formed shed vortices. In fact, in Case F, the shear layers are so close that the roll-up is almost entirely prevented and the “shed” vortices form and remain within the shear layer until the shear layer breaks up. Spectra of the cross-stream velocity at x/D = 4.0 for Cases D & F, both showed a peak. However, Case F showed a broader peak indicating larger fluctuations in the shedding period.

The shedding in Case F was found to be intermittent. The shed vortices were about 1.0D to 4.0D long in the spanwise direction (with some of them occurring at a noticeable angle to this direction). Quiescent regions, between regions of shedding activity, both in time and in the z direction were observed. The former are an indication of intermittency in the shedding process. The active/quiescent

regions may be an indication that boundary layer disturbances aid/inhibit vortex shedding. This aspect is being investigated.

To obtain a better understanding of the initiation of the shedding process, shedding was first examined in a far simpler case, that is, the flow past a cylinder at a low Reynolds number. It was determined with the aid of velocity vectors at different phases of the shedding process that the initial circulatory flow in this case is caused by the induced velocities of the previous two shed vortices (positive and negative) and the forward flow in the shear layer. The pressure minimum associated with the newly formed vortex appears later.

Velocity vector and pressure contour plots were also used in the case of the flat plate to understand the shedding process in Cases A & F (low and high θ/D cases) and compare it to that of the cylinder. The data showed that the essential attributes of the process were quite similar to that found in the cylinder wake. The induced velocity fields of the previous two shed vortices and the forward flow in the shear layer and further away from the centerline result in circulating flow very near the base.

The range of values over which D & θ vary, in the six computations used here, is significant. It permits the development of a functional relationship (model) between the shedding frequency and Re_{θ} and Re_D. A "power-law" relationship has been developed here. The associated exponents (α and β) were estimated from the DNS data. The model shows a weak dependence on Re_{θ} (α = 0.1156) and a nearly linear dependence on Re_D (β = 1.1520). The computed data and the predictions of the model were found to be in agreement, indicating the validity of the model for the range of Re_{θ} and Re_D considered.

The effect of changing the ratio θ/D on the time-averaged, near-wake velocity statistics is also provided here (Cases D & F). It was found that increasing θ/D resulted in weakened reverse flow that persists for longer distances (in terms of the thickness of the plate). Contours of time-averaged spanwise vorticity showed that increasing θ/D resulted in decreasing the separation between the upper and lower shear layers and increasing their streamwise extent. Peak cross-stream intensity along the wake centerline was substantially lowered with increasing θ/D because of weaker shed vortices. The peak streamwise intensity was also lowered but by a much smaller factor because of the turbulent nature of the separated boundary layer (and thus the inherited streamwise intensity). Interestingly, distributions of the components of velocity and fluctuating kinetic energy and shear stress were found to remain topologically quite similar with changing θ/D, however, the scales and locations of the various features such as maxima/minima are considerably different.

REFERENCES

CHEVRAY, R. & KOVAZNAY, L. S. G. 1969 Turbulence measurements in the wake of a thin flat plate. *AIAA Journal*, Vol. 7, 1641.

DONG, S., KARNIADAKIS, G. E., EKMEKCI, A. & ROCKWELL, D. 2006 A combined direct numerical simulation-particle velocimetry study of the turbulent near wake. *Journal of Fluid Mechanics*, Vol. 569, 185.

JEONG, J. & HUSSAIN, F. 1995 On the identification of a vortex. *Journal of Fluid Mechanics*, Vol. 285, 69.

PERRY, A. E., CHONG, M. S. & LIM, T. T. (1982) The vortex shedding process behind two-dimensional bluff bodies. *Journal of Fluid Mechanics,* **116**, 77.

PERRY, A. E. & STEINER, T. R. (1987) Large-scale vortex structures in turbulent wakes behind bluff bodies. Part 1. Vortex formation processes. *Journal of Fluid Mech*anics, **174**, 233-270.

RAI, M. M. 2008 Towards direct numerical simulations of turbulent wakes. Paper 2008-0544, 46th AIAA Aerospace Sciences Meeting, 2008, Reno, Nevada.

RAI, M. M. 2010a A computational investigation of the instability of the detached shear layers in the wake of a circular cylinder. *Journal of Fluid Mechanics*, Volume 659, pp. 375-404.

RAI, M. M. 2010b Direct numerical simulation of transitional and turbulent Flow on a turbine Airfoil. *AIAA Journal of Propulsion & Power*, Volume 26, (3), 587.

RAI, M. M. 2011 Flow physics and self-similarity in the turbulent near wake of a flat plate. Paper 2011-3575, 41st AIAA Fluid Dynamics Conference, Honolulu, Hawaii.

RAI, M. M. 2013 Flow physics in the turbulent near wake of a flat plate. *Journal of Fluid Mechanics*, Volume 724, 704.

RAI, M. M. 2014 Flow Phenomena in the very near wake of a flat plate with a circular trailing edge. *Journal of Fluid Mechanics*, Volume 756, 510.

Rai, M. M. 2015 Detached shear-layer instability and entrainment in the wake of a flat plate with turbulent separating boundary layers. *Journal of Fluid Mechanics*, Volume 774, 5.